An Experimental and Numerical Investigation of Flow Over a Hydrofoil in Transient Regimes Based on Wall-Pressure Analysis

Antoine Ducoin, Jacques-André Astolfi, François Deniset, Jean-François Sigrist, Vincent Soyer

To cite this version:

Antoine Ducoin, Jacques-André Astolfi, François Deniset, Jean-François Sigrist, Vincent Soyer. An Experimental and Numerical Investigation of Flow Over a Hydrofoil in Transient Regimes Based on Wall-Pressure Analysis. ASME 2008 Pressure Vessels and Piping Conference, Jul 2008, Chicago, IL, United States. pp.239-247, 10.1115/PVP2008-61575 . hal-04642668

HAL Id: hal-04642668
https://hal.science/hal-04642668v1

Submitted on 19 Jul 2024

Proceedings of PVP2008
2008 ASME Pressure Vessels and Piping Division Conference
July 27-31, 2008, Chicago, Illinois, USA

AN EXPERIMENTAL AND NUMERICAL INVESTIGATION OF FLOW OVER A HYDROFOIL IN TRANSIENT REGIMES BASED ON WALL-PRESSURE ANALYSIS

Antoine Ducoin, Jacques André Astolfi, François Deniset
Institut de Recherche de l'Ecole Navale EA 3634
Ecole Navale
29240 Brest Armées
France
Email: antoine.ducoin@ecole-navale.fr

Jean-François Sigrist, Vincent Soyer
DCNS Propulsion
44620, La Montagne
France
Email: jean-francois.sigrist@dcnsgroup.com

ABSTRACT

The present study is developed within the general framework of marine structure design of lifting bodies, operating in transient regimes. The study concerns the experimental and numerical investigations of time-space distribution of the wall pressure field on a NACA66 hydrofoil in forced ramping motion. The angle of incidence varies from 0° *to* 15° *beyond stall. Experiments in a hydrodynamic tunnel and corresponding RANSE based code calculations are carried out for various pitching velocities. Transducers are located along the chord of the hydrofoil. The numerical approach is conducted in turbulent regime using recent laminar to turbulent transition model. Global coefficients are analyzed in order to quantify the transient effects. The comparison of calculated to measured local wall pressures on the suction side leads to the identification of the effect of pitching velocity on hydrodynamic loading. Moreover, the consequences of pressure fluctuations induced by the laminar to turbulent transition are highlighted. The evolutions of transition, laminar bubble and leading and trailing edge detachments are discussed in the context of naval applications.*

INTRODUCTION

The load prediction of lifting bodies such as rudders, stabilizers or marine propellers in forced motion of large amplitude is fundamental in the context of marine design. It requires a good understanding of phenomena such as transition, turbulence and stall ([1]). The knowledge of the pressure field distribution on the body and its evolution in time can then bring new elements in the understanding of the phenomena of dynamic loading. It includes the boundary layer study in forced unsteady regime which has always been the object of many researches, including its prediction in RANSE based codes in the context of industrial applications. [2] has shown the accuracy of RANSE codes to predict hydrodynamic loading in cases of low angles of incidence, and highlighted the turbulence model dependency when separation becomes high. This has been studied by [3] on a NACA0015 and a NACA0012. The influence of pitching velocities can be also of primary importance on loading prediction. This has been studied numerically by [4] in the case of low Reynlods numbers. Inertia effects are increasing with pitching velocities and the authors include non-dimensionnalized parameters useful in transient regimes which are performed in the present paper. An experimental study is presented in [5] for an oscillating airfoil at various reduced frequency and at $Re = 1.35 \times 10^5$. For small values of reduced frequencies, boundary layer events produce variations in lift, drag and moment coefficient. As well, it has some influence on boundary layer transition caused by laminar separation which is delayed and promoted when reduced frequency increase. The lift coefficient and lift-curve slope has also slight improvement but it has been shown that the laminar bubble length is insensitive to reduced frequency. Recent works focus on the impact of transition modeling in RANSE based codes([6], [7], [8]). It appears to have impact on stall and loading prediction. [9] show that fully turbulent computations over predict lift and drag. [6]

include transition model and show the impact on hydrodynamic coefficient.

The present paper focuses on the spatio-temporal evolution of the wall pressure field of an hydrofoil arising from transient pitching motion at $Re = 0.75 \times 10^6$. Both experimental and numerical approaches has been developed. The experiment is based on the wall pressure measured by transducers on several points at the suction side of an hydrofoil. Computations are led with the CFD RANSE based code CFX.
The first aim of this study is a better understanding of hydrodynamic loading responses on flow phenomena like transition and of laminar separation induced transition. Another challenging task is to verify the accuracy of the RANS simulation to predict them, and to evaluate their limitations.

The flow is first studied in the case of a slow rotation velocity based on wall pressure near the leading edge and the trailing edge and numerical separation and transition localization on the hydrofoil. Then the influence of the 4 rotation velocities on the boundary layer events is analyzed with CFD results. Then Local wall pressures are integrated in order to define a suction side loading which will allow to compare measurement and calculation on the basis of a reconstructed hydrodynamic loading. The global numerical coefficient can then be analyzed and dynamic contribution of the pitching velocity is highlighted.

EXPERIMENTAL SET UP

Measurements are carried out in the cavitation tunnel at IRENav. The test section is 1 m long and has a 0.192m square section. It allows to control the velocity range between 0 and 15m/s and pressure range from 30 mbar to 3 bars.The hydrofoil is mounted horizontally in the tunnel test section. The chord is c=0.150 m and the span is b=0.191 m. The camber is about 2% to 50% from the leading edge([10]).

Pressure measurements are carried out using seventeen piezo-resistive transducers (Keller AG 2 MI PAA100-075-010) of 10 bars maximum pressure. The pressure transducers are mounted into small cavities with a 0.5 mm diameter pinhole at the hydrofoil surface. The wall pressure spectrum measured by the transducer is attenuated from the theoretical cut off frequency $f_c = 9152 Hz$. Experiments are led with a sample frequency of f=20kHz.

The transducer locations are given in Figure 1. As shown, one set of ten transducers is aligned along the chord of length on the suction side, starting from the leading edge at reduced coordinate x/c=0.05 up to the trailing edge at coordinate x/c=0.90 with a step of 0.10 c from x/c=0.10.

Two sets of three transducers are arranged in parallel to this line in order to analyze three-dimensional effects. The transducers responses are found to be linear and the coefficients of the linear regression are used to convert Volts in Pascals. To control any deviation during the experiments, the calibration procedure is performed systematically before and after each series of measurements. Signals from the wall-pressure transducers are amplified and collected through a simultaneous sampling 16 channel, 16 bit A/D digitizer VXI HPE1432A, having maximum available sampling frequency of 51.2 kHz.

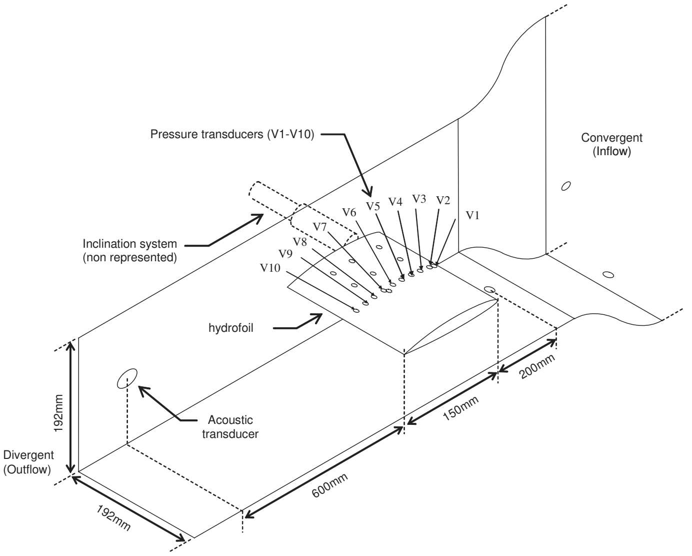

Figure 1. HYDROFOIL INSTRUMENTATION AND TUNNEL TEST SECTION

The nominal free stream velocity U_∞ was 5 m/s, corresponding to a Reynolds number based on the foil chord length of $Re = 0.75 \times 10^6$. The hydrofoil rotated about an axis located at 25% from the leading edge. The angle of incidence vary from $0°$ to $15°$ then come back to $0°$, with at least 2 periods of accelerations and 2 periods of deceleration.

As shown in figure 2, four rotation velocities are defined, from a considered slow rotation velocity to a high rotation velocity.

The average rotation velocity is defined as:

$$\dot{\alpha} = 2\alpha_{max}/t_f \tag{1}$$

with t_f the total time of transient motion. Let's introduce a similarity parameter based on the chord length c and the upstream velocity U_∞:

$$\dot{\alpha}^* = \frac{\dot{\alpha} \times c}{U_\infty} \tag{2}$$

FLOW MODELING AND NUMERICAL RESOLUTION

The fluid flow is described with the mass and momentum conservation equations which read for an incompressible and vis-

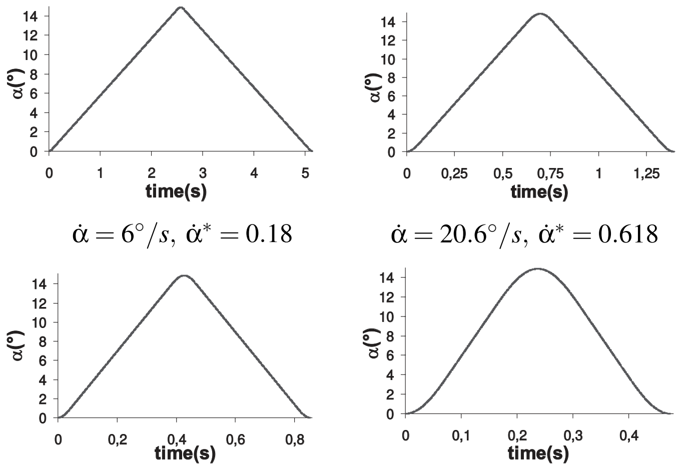

$\dot{\alpha} = 6°/s,\ \dot{\alpha}^* = 0.18$ $\dot{\alpha} = 20.6°/s,\ \dot{\alpha}^* = 0.618$

$\dot{\alpha} = 35°/s, \dot{\alpha}^* = 1.05$ $\dot{\alpha} = 63°/s, \dot{\alpha}^* = 1.89$

Figure 2. ANGLE OF INCIDENCE VERSUS TIME FOR 4 PITCHING VELOCITIES

cous fluid:

$$\frac{\partial v_j}{\partial x_j} = 0 \tag{3}$$

$$\frac{\partial(\rho v_i)}{\partial t} + \frac{\partial(\rho v_i v_j)}{\partial x_j} = -\frac{\partial p}{\partial x_i} + \mu \frac{\partial^2 v_i}{\partial x_j \partial x_j} \tag{4}$$

where v, ρ and μ are the velocity, density and dynamic viscosity of the fluid. The fluid problem is solved with the finite volume technique ([11]), using the CFD code CFX. Equations of mass and momentum are integrated over a control volume Ω_F of boundary $\partial\Omega_F$, using the Leibnitz rule and the Gauss theorem. It is then discretized using a finite volume method. The fluid domain is divided into elementary fluid cells, for which an integrated conservation equation is written. The time dependent terms are approximated by an Euler scheme, and convective and diffusive terms are calculated using finite difference approximations. Nodal values are computed with a high resolution upwind scheme. The advection scheme for a given quantity ϕ is implemented into the CFD code and can be written as:

$$\phi_p = \phi_{up} + \beta \nabla\phi \Delta \vec{r} \tag{5}$$

where ϕ_p and ϕ_{up} are respectively the values of ϕ at the integration point P and at the upwind node (depending on the flow direction), β is a relaxation coefficient ranging between 0 and 1 and $\vec{r}$ is the vector from the upwind node to the integration point P.

Turbulence and transition modeling

The calculations are led with the CFD RANSE based code CFX. The $k-\omega SST$ model appears to be an accurate turbulence model for boundary layer detachment prediction ([12], [13], [14]).
The $k-\omega SST$ turbulence model is coupled with a transition model $\gamma - Re_\theta$ which uses experimental correlations based on local variables([15], [16], [17]). The model is based on two transport equations. The first one is for intermittency γ which triggers the transition process:

$$\frac{\partial(\varphi\gamma)}{\partial t} + \frac{\partial(\varphi v_j \gamma)}{\partial x_j} = P_\gamma + E_\gamma + \frac{\partial}{\partial x_j}\left[(\mu + \frac{\mu_t}{\sigma_f})\frac{\partial\gamma}{\partial x_j}\right] \tag{6}$$

where P_γ and E_γ are the transition sources based on empirical correlations. μ_t is the friction velocity.

The transport equation for the transition momentum thickness Reynolds number $\overline{Re\theta_t}$ is given by:

$$\frac{\partial\left(\rho\overline{Re_{\theta t}}\right)}{\partial t} + \frac{\partial\left(\rho U_j \overline{Re_{\theta t}}\right)}{\partial x_j} = P_{\theta t} + \frac{\partial}{\partial x_j}\left[\sigma_{\theta t}\left(\mu + \mu_t\right)\frac{\partial \overline{Re_{\theta t}}}{\partial x_j}\right] \tag{7}$$

with $P_{\theta t}$ a source term which force $\overline{Re_{\theta t}}$ to match the local value of $Re_{\theta t}$ based empirical correlation. $\sigma_{\theta t}$ is a source term diffusion control.
In this formulation, only local information is used to activate the production term in the intermittency equation. This model allows to capture major transition effects and is accurate in the case of separation induced transition. The intermittency is modified to accept values larger that 1 at separation in order to have a correct transition length. Complete transition formulation is given in [17].

Boundary conditions and Discretization

The domain dimensions corresponds to the tunnel test section at IRENav. The ratio between the square section h and the chord length c is h/c=0.7. The inlet velocity is set to U=5m/s and the taken outlet reference pressure is set to 0. Symmetries conditions are set on horizontal wall and a no slip condition is imposed on the hydrofoil surface. Transients computations are initialized with a stationary converged computation. As shown in figure 3, the mesh is composed of 66,000 elements and 50 layers are used in the structured near wall zone. The other part of the domain is discretized with unstructured triangle elements. The boundary layer is discretized in order to satisfies $y^+ = \frac{y u_\tau}{\nu} = 1$. This ensure low Reynolds resolution. Mesh refinements is done at the leading edge, the trailing edge and in the wake. The hydrofoil motion is taken into account with boundary condition modification at wall. To do that, mesh coordinates are calculated at each time step and

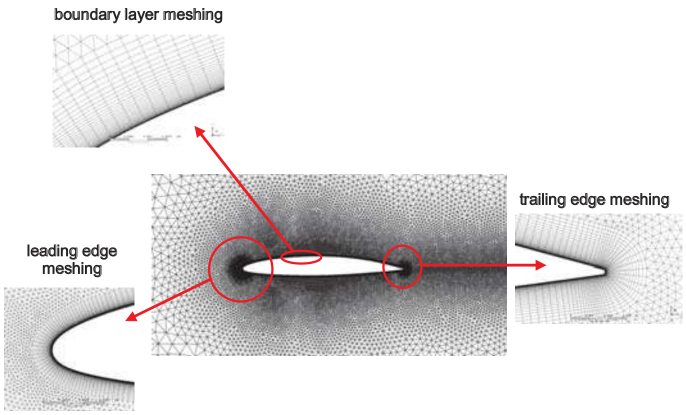

Figure 3. HYDROFOIL MESH

Table 1. LIFT AND DRAG COEFFICIENT CONVERGENCE ACCORDING TO BOUNDARY LAYER RESOLUTION, $\alpha = 6°$, $Re = 0.75 \times 10^6$

Boundary layer resolution	$y+$	Cl	(%)	Cd	(%)
Wall function	50	0.9661	3.3	0.0144	14.6
Low Reynolds	2	0.9529	1.9	0.0163	3.2
Low Reynolds	1	0.9503	1.6	0.0164	2.7
Low Reynolds	0.5	0.9362	0.1	0.01676	0.5
Low Reynolds	0.3	0.9353	0	0.01686	0

Table 2. LIFT AND DRAG COEFFICIENTS AS A FUNCTION OF NUMBER OF ELEMENTS $\alpha = 6°$, $Re = 0.75 \times 10^6$

$Nfoil$	$Ntotal$	Cl	(%)	Cd	(%)
50	18 000	0.9915	4.3	0.02198	34.2
100	23 000	0.9545	0.4	0.01987	21.3
200	40 000	0.9477	0.3	0.01719	4.9
400	64 000	0.95026	0.1	0.0164	0.1
$Nmax = 800$	1 100 000	0.95082	0	0.01638	0

the whole domain is then meshed again. This technique used a diffusivity applied in the mesh displacement equation which induced a mesh stiffness([18], [19], [20]). This one is set to be inversely proportional to the wall distance in order to limit mesh distortion near the wall region. The Navier-Stokes equations are resolved in an arbitrary referential with the ALE formulation:

$$w(x^*,t) = v(X,t) - v_R(x,t) \tag{8}$$

Where X is linked to the material coordinate and x to the space coordinates, $w(x^*,t)$ is the mesh strain velocity.
Momentum equation is modified as follows:

$$\rho\frac{\partial v_i}{\partial t} + \rho\,(v_j - v_{Rj})\,\frac{\partial v_i}{\partial x_j} = \frac{\partial p}{\partial x_i} + \mu\frac{\partial^2 v_i}{\partial x_j \partial x_j} \tag{9}$$

Computation is performed in two steps:

in the Lagrangian step the reference system follows the structure, $((v_j - v_{Rj}) = 0)$,
in the advection step, the mesh is fixed and the only advection term is resolved, $((v_j - v_{Rj}) \neq 0)$.

Mesh convergence is carried out on hydrodynamic coefficients for an angle of attack of 6° and a stationary flow. Table 1 summarized the lift and drag coefficients for each tested case. The thickness of the structured mesh near the wall and the aspect ratio between structured and unstructured meshes have been conserved. It appears that wall function predicts quite well the lift coefficient compared to the low Reynolds resolution $y_+ = 0.3$ taken as a reference. On the other hand, the wall function over predict the drag coefficient of about 15 percent. This is due to the contribution of wall shear to the drag coefficient. The influence of the number of elements has been investigated in Table 2.N_{foil} is the number of nodes at hydrofoil's surface and N_{total} is the number of elements. The lift coefficient converges very fast assumed to N_{foil}, from 100 elements. on the other hand, the drag coefficient converges from 200 elements.

Temporal discretization has been set according to CFL number with fixed spatial mesh. Figure 4 show pressure coefficient located at x/c=0.1 versus time for pitching motion from 0° to 15°, $\dot{\alpha}^* = 0.18$. We focus on the non linear behaviour which appears to be associated to transition which needs a high temporal discretization level. $\Delta t = 0.001s$ has been chosen because lower time steps gives identical results. In the same way, Figure 5 show that the leading edge separation is very sensitive to Δt. With the lower Δt, there is advance in separation. Simulation

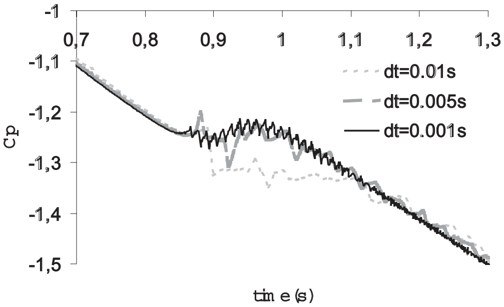

Figure 4. PRESSURE COEFFICIENTS VERSUS TIME FOR VARIOUS TIME STEPS IN TRANSITION ZONE

time and pitching velocities are modified for the dynamic study so time step must verify $\frac{\Delta t}{t_f} > 5 \times 10^{-4}$. This ensure a minimum number of time steps for each computation.

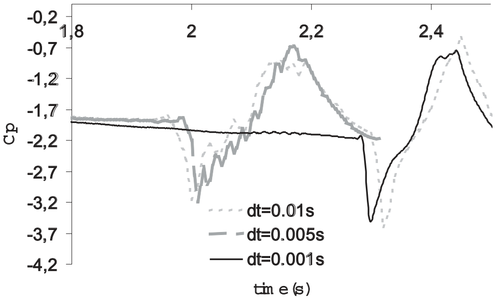

Figure 5. PRESSURE COEFFICIENTS VERSUS TIME FOR VARIOUS TIME STEPS IN LEADING EDGE SEPARATION ZONE

RESULTS AND DISCUSSION

Figure 6 shows a typically evolution of the measured pressure coefficient at x/c=0.3 during the transient motion from 0° to 15° compared to the computed one. As shown, there is a good agreement between the experimental and the numerical results except high frequency fluctuations which are not observed by the computation. From 0° to 5°, the pressure decreases with low fluctuations. At 5°, the pressure stops to decrease and shows an inflection with a high level of fluctuations. Then the pressure continues to decrease with significant fluctuations, whose intensity increases from 6° to 13°. A more precise analysis has shown that these fluctuations are quasi-periodic and then can be related to vortex shedding downstream a laminar separation bubble as shown later. From 13° a strong pressure overshoot is observed, then low frequency fluctuations with large amplitude are observed resulting of stall. The relative complex characteristic of the wall pressure evolutions comes from the various features of the boundary layer flow during foil rotation.

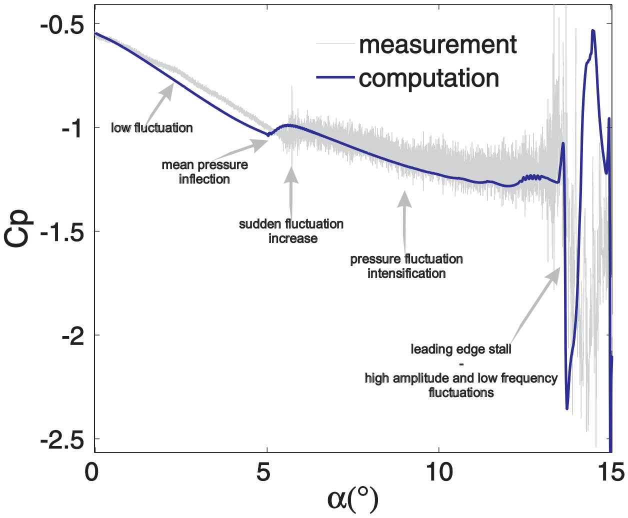

Figure 6. EXPERIMENTAL AND NUMERICAL PRESSURE COEFFICIENT AS FUNCTION OF THE ANGLE OF INCIDENCE AT x/c=0.3 DURING THE TRANSIENT MOTION

Flow analysis

As an example, the flow is analyzed for the lowest pitching velocity $\dot{\alpha}^* = 0.18$. Velocity streamlines are determined from computations, which allows to have a general view of the flows including separation and reversed flow (Figure 7). As shown at 0°, a reversed flow is located at x/c=0.8 resulting from a Laminar Separation Bubble (LSB) inducing a transition to turbulent flow at reattachment. The displacement of LSB toward the leading edge zone can be seen up to 5°. At 5° the trailing edge LSB is replaced by a leading edge LSB as show in Figure 7 at $\alpha = 11^\circ$. Then stall is observed at 13.3° with leading edge vortex shedding. A maximum under-pressure appears at $\alpha = 13.9^\circ$. Then two contra-rotative vortices are shed from the trailing edge. This scenario is repeated periodically 3 times. A reverse scenario is observed during downward rotation of the hydrofoil.

Separation points and transition location have been located using wall shear stress equal 0. The transition point is defined as the reattachment turbulent point. Figure 8 summarizes the separations and transition location from $\alpha = 0^\circ$ to 12° (before stall). The vertical axis is the x/c location on chord from leading edge (x/c=0) to trailing edge (x/c=1). The trailing edge separation point is located very close to the trailing edge for 0°, and moves slowly toward the leading edge when the angle of incidence increases. For $\alpha = 0^\circ$ to 5° the two characteristics points (separation and reattachment) are between $(x/c)_{sep}$=0.85 to 0.69 and $(x/c)_{reattach}$=0.74 to 0.66. As a matter of fact, global length of LSB tends to decrease as α increases. At $\alpha = 5^\circ$, the trailing edge LSB disappears and a shorter LSB induced by higher pressure gradient is formed at the leading edge which induces a sudden move of the transition location from x/c=0.65 to x/c=0.08. As well, the trailing edge separation suddenly moves from x/c=1 to x/c=0.9.

Figure 9 shows the experimental and computed wall pressure coefficient evolutions at x/c=0.8 **(a)** and x/c=0.3 **(b)**. First, wall pressure coefficient at x/c=0.8 shows a sudden increase at $\alpha = 2^\circ$. According to figure 8, the LSB turbulent reattachment point is just passing up to this point at $\alpha = 2^\circ$. Measurements show an increase of pressure fluctuations around this angle of incidence while a maximum is around $\alpha = 3^\circ$. For both computation and measurement, there is a global pressure inflection at $\alpha = 5^\circ$ as transition is passing near the leading edge. Figure 9 **(a)** and **(b)** show that the pressure fluctuations measured increase highly at this angle and continue to increase slowly up to $\alpha = 12^\circ$.

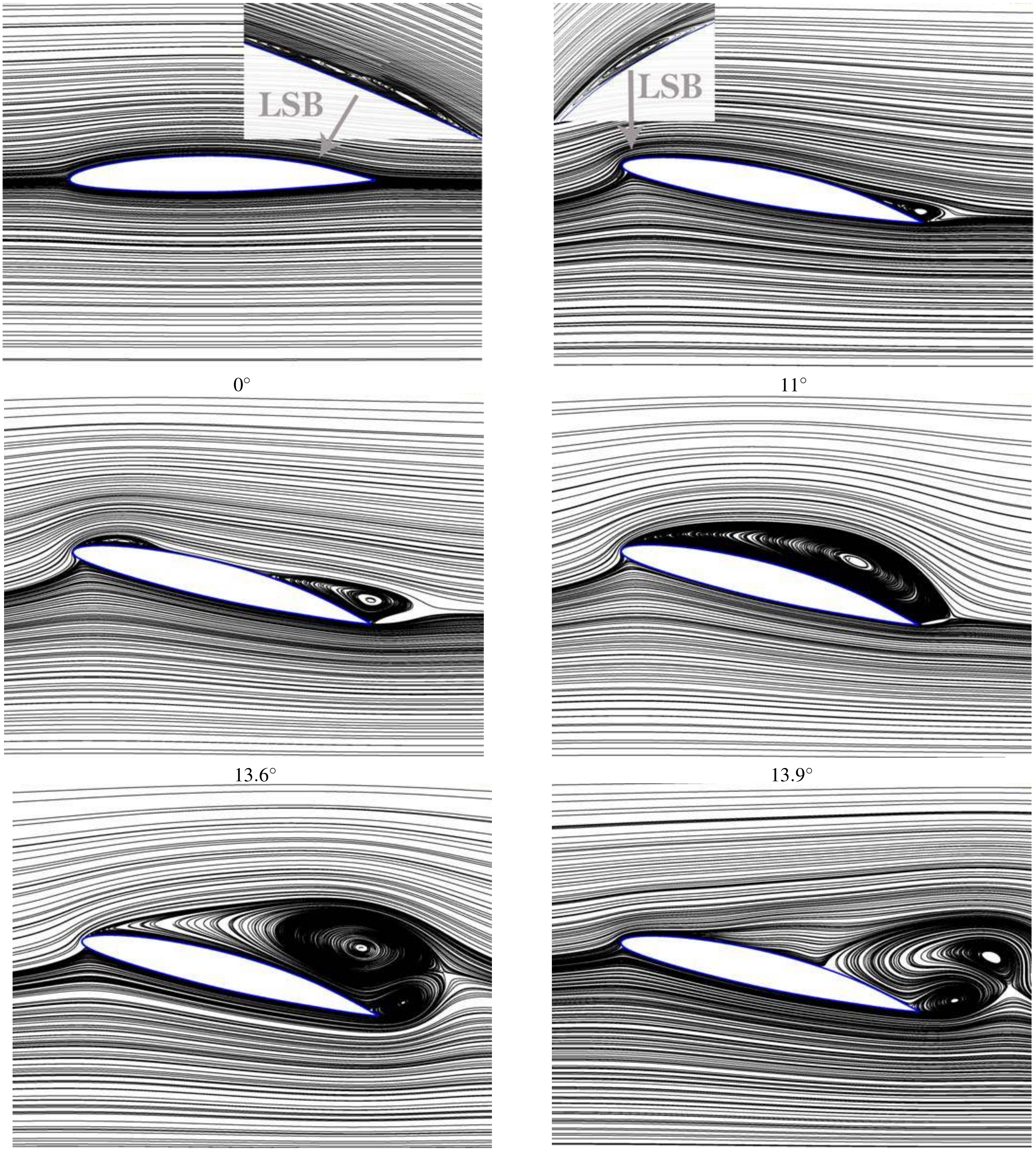

0°

11°

13.6°

13.9°

14.2°

14.5°

Figure 7. FLOW VISUALIZATIONS, $\dot{\alpha}^{*} = 0.18$

At the same time, wall pressure on x/c=0.8 reaches a maximum value at $\alpha = 10°$ which corresponds to the trailing edge separation, see figure 8.

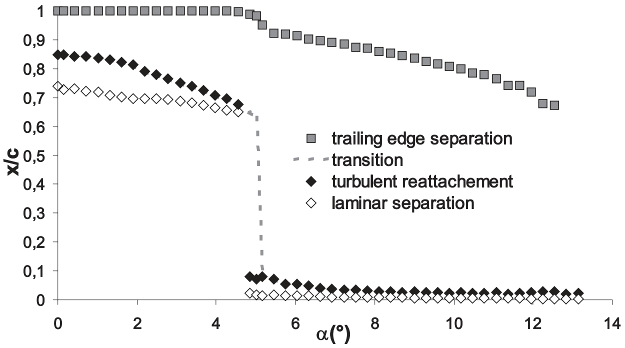

Figure 8. SEPARATION POINTS AND TRANSITION LOCATION AT SUCTION SIDE AS A FUNCTION OF THE ANGLE OF INCIDENCE

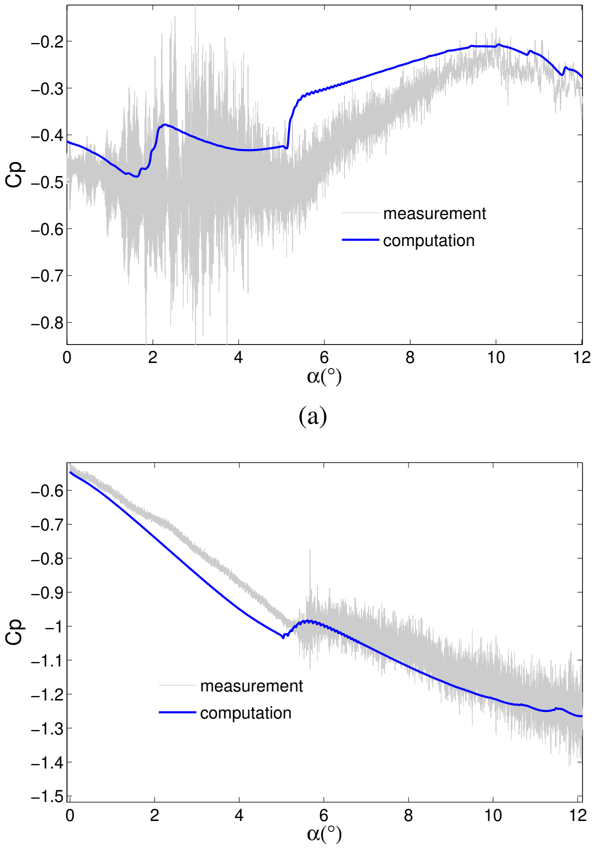

(b)

Figure 9. PRESSURE COEFFICIENT AT $\dot{\alpha}^* = 0.18$, α=0 to 12° BEFORE STALL: **(a)** x/c=0.8 AND **(b)** x/c=0.3 AS FUCTION OF THE ANGLE OF ATTACK

Dynamic effects of pitching velocity on boundary layer events

Figure 10(a) represents the transition and the trailing edge separation and Figure 10(b) the LSB length , for the considered pitching velocities. It is observed that transition is delayed when pitching velocity increases. Trailing edge separation point is delayed which induces a higher lift coefficient before stall. Pitching velocity does not have impact on the LSB size. Few variation appears when it formed (delayed with transition as shown on transition point location on chord) but from $\alpha = 7°$ to stall, bubble lengths are the same. This correlation agrees with the idea that high pitching velocities delayed the separation induced transition phenomenon whereas boundary layers thickness and separation length are conserved. All these points influences hydrodynamic loading of the foil.

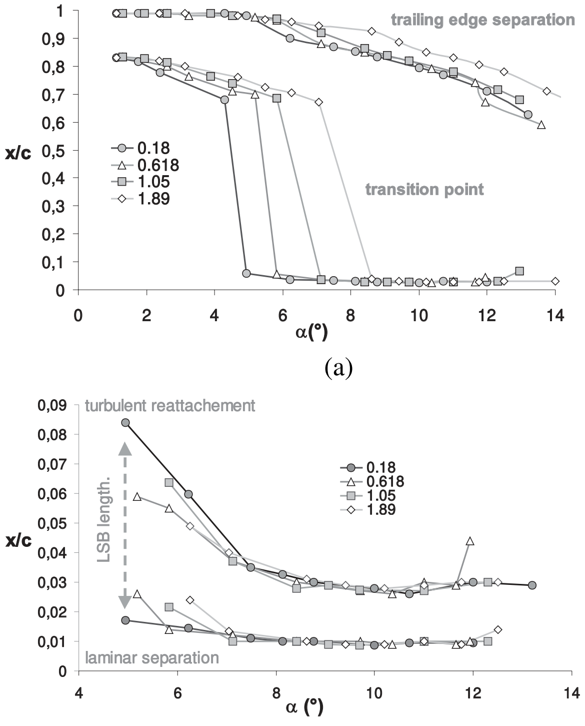

(b)

Figure 10. **(a)**: BOUNDARY LAYER SEPARATION AT LEADING EDGE AND TRANSITION LOCATION ON CHORD DURING PITCHING MOTION, **(b)**: LSB LENGTH AT LEADING EDGE FOR VARIOUS $\dot{\alpha}^*$

Suction side loading analysis

Based on available experimental data, an analysis of suction side loading can be done by summing pressure coefficient on the suction side. The approximation can be written as:

$$C_l^+(t) = \sum_{i=2}^{10} C_p(\frac{x_i}{c},t)\,\Delta(\frac{x_i}{c}) \qquad (10)$$

where $C_p(\frac{x_i}{c},t)$ is the pressure coefficient at location $\frac{x_i}{c}$ and $\Delta(\frac{x_i}{c})$ is the non dimensional distance between two consecutive transducers. The procedure is applied to numerical data for comparison. Figure 11 shows the results obtained for the 4 rotation velocities. As shown, there is a good agreement between measurements and computations. The difference is very weak at the beginning of pitching and the inflection is accurately predicted by the transition model which appears at 5° for the lowest pitching velocity. It is delayed when pitching velocity increases and disappears even completely at the highest pitching motion for both approach. High amplitude fluctuations at low frequency induced by leading edge vortex shedding is over predicted by computation but starts at an angle of incidence very close to measurement. The return to 0° shows hysteresis induced by a delay in the reattachment. Again, computations agree well to measurements even if the model tends to over predict the loading when the pitching velocity increases.

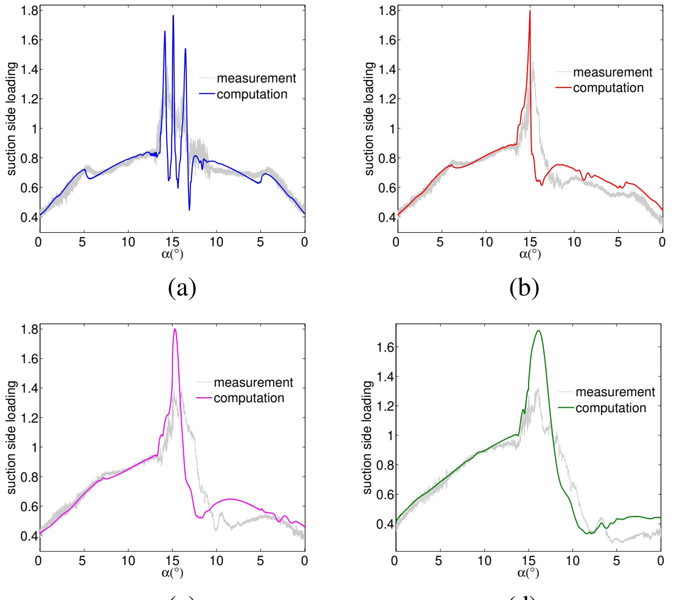

(a) (b)

(c) (d)

Figure 11. SUCTION SIDE LOADING DURING PITCHING MOTION: $\dot{\alpha}^* = 0.18$ **(a)**, $\dot{\alpha}^* = 0.618$ **(b)**, $\dot{\alpha}^* = 1.05$**(c)** AND $\dot{\alpha}^* = 1.89$ **(d)**

Then it allows to analyze the influence of pitching velocity on global coefficients obtained by computations.

Dynamic effects: numerical lift coefficient

Figure 12 shows the numerical lift coefficient evolution as a function of the angle of incidence during pitching motions. Transition model appears to have a significant impact on lift when the rotation velocity is weak. An inflection is followed by a slope modification at 5° for $\dot{\alpha}^* = 0.18$ and 7° for $\dot{\alpha}^* = 1.05$ which tends to disappear for $\dot{\alpha}^* = 1.89$. Then lift amplitude before stall is higher at high velocities. Stall appear at 13.3° for the weakest velocity and is delayed at 14.4° for the highest velocity. It is shown that high lift fluctuations induced by leading edge vortex shedding appears at all pitching velocities, about three times for the weakest pitching velocity and one time for the other ones. The reattachment is also delayed with high velocities which induce hysteresis. As a consequence, lift evolution is symmetric for $\dot{\alpha}^* = 0.18$ where the reattachment is located for $C_L = 1.33$ whereas $C_L = 0.16$ for $\dot{\alpha}^* = 1.89$.

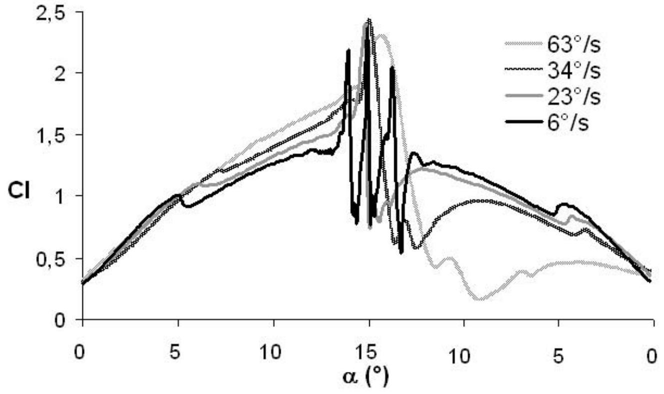

Figure 12. LIFT COEFFICIENT AS A FUNCTION OF THE ANGLE OF INCIDENCE, $0-15°$ AND RETURN TO $0°$, FOR 4 PITCHING VELOCITIES

CONCLUSION

The spatio-temporal evolution of the wall pressure field around an hydrofoil arising from a transient pitching motion at a $Re = 0.75 \times 10^6$ has been carried out for both experimental and numerical approaches. Four pitching velocities have been studied from a slow one $\dot{\alpha}^*$=0.18 to a high one $\dot{\alpha}^*$=1.89. The repartition of transducers location along the suction side of the hydrofoil at reduced coordinates from x/c=0.10 to x/c=0.90 with a step of 0.10 c has led to both global and local analysis.

Local wall pressure coefficients near the trailing edge at x/c=0.8 and near the leading edge at x/c=0.3 allow to know the transition behaviour. There is a good agreement between measurements and calculations. Trailing edge separation is accurately predicted in agreement with the lift inflection after that the boundary layer transition passes from the trailing edge toward the the leading edge. The author associates those fluctuations to vortex shedding of a laminar separation bubble. Based on the good agreements between experimental and numerical results, the influence of pitching velocity has been studied. Higher pitching velocities show a delay of transition and LSB length is constant. Suction side loading shows a good agreement between measurements and computations. Global effect of transition are accurately predicted by the RANSE code whereas wall pressure fluctuations are not captured. Numerical lift coefficients for the various pitching velocities highlight the impact of transition for slow motions which induces a significant lift coefficient slope modification at $\alpha = 5°$. Higher pitching velocities has an impact on boundary layer transition effect on hydrofoil loading which induced a higher value before stall. During the the return step to $\alpha = 0°$, an hysteresis effect induced by the massive stall is very marked for the highest velocity .

ACKNOWLEDGMENT

The authors gratefully acknowledge the technical staff of IRENav for its contribution to the experimental set up.

REFERENCES

[1] Triantafyllou, G., Triantafyllou, M., and Grosenbaugh, M., 1993. "Optimal thrust development in oscillating foils with application to fish propulsion.". *Journal of Fluids and Structures,* **7**(2), pp. 205–224.

[2] Srinivasan, G., Ekaterinaris, J., and McCroskey, W., 1995. *Evaluation of Turbulence Models for Unsteady Flows of an Oscillating Airfoil*. Pergamon; National Aeronautics and Space Administration; National Technical Information Service, distributor.

[3] Barakos, G., 2000. "Unsteady separated flows over manoeuvring lifting surfaces". *Philosophical Transactions: Mathematical, Physical and Engineering Sciences,* **358**(1777), pp. 3279–3291.

[4] Hamdani, H., and Sun, M., 2000. "Aerodynamic forces and flow structures of an airfoil in some unsteady motions at small Reynolds number". *Acta Mechanica,* **145**(1), pp. 173–187.

[5] Lee, T., and Gerontakos, P., 2004. "Investigation of flow over an oscillating airfoil". *Journal of Fluid Mechanics,* **512**, pp. 313–341.

[6] Shelton, A., Abras, J., Hathaway, B., Sanchez-Rocha, M., Smith, M., and Menon, S., 2005. "An Investigation of the Numerical Prediction of Static and Dynamic Stall". *Proceedings of the 61" American Helicopter Society Annual Forum, Grapevine,* **10**(10), p. 6.

[7] Studer, 2005. "Experimental and numerical study of laminar-turbulent transition in unsteady flow". PhD thesis, Ecole nationale supérieure de l'aéronautique et de l'espace.

[8] Richez, F., Mary, I., Gleize, V., and Basdevant, C., 2006. "Near stall simulation of the flow around an airfoil using zonal RANS/LES coupling method". *36 th AIAA Fluid Dynamics Conference and Exhibit*.

[9] Smith, M., Wong, T., Potsdam, M., Baeder, J., and Phanse, S., 2004. "Evaluation of CFD to Determine Two-Dimensional Airfoil Characteristics for Rotorcraft Applications". *American Helicopter Society 60 thAnnual Forum, Baltimore, MD, June*.

[10] Leroux, J., Coutier-Delgosha, O., and Astolfi, J., 2005. "A joint experimental and numerical study of mechanisms associated to instability of partial cavitation on two-dimensional hydrofoil". *Physics of Fluids,* **17**, p. 052101.

[11] Ferziger, J., and Peric, M., 2002. *Computational methods for fluid dynamics*. Springer New York.

[12] Menter, F., 1993. "Improved Two-Equation k-Turbulence Models for Aerodynamic Flows". *NASA Technical Memorandum,* **103975**, p. 34.

[13] Menter, F., Kuntz, M., and Langtry, R., 2003. "Ten Years of Industrial Experience with the SST Turbulence Model". *Turbulence, Heat and Mass Transfer,* **4**, pp. 625–632.

[14] Haase, W., Aupoix, B., Bunge, U., and Schwamborn, D., 2006. "FLOMANIA-A European Initiative on Flow Physics Modelling". *Berlin: Springer, 2006. ISBN 3-540-28786-8*.

[15] Abu-Ghannam, B., and Shaw, R., 1980. "Natural transition of boundary layers-The effects of turbulence, pressure gradient, and flow history". *Journal of Mechanical Engineering Science,* **22**, pp. 213–228.

[16] Steelant, J., and Dick, E., 1996. "Modelling of bypass transition with conditionned intermittency transport equation". *International journal for numerical methods in fluids,* **23**, pp. 193–220.

[17] Menter, F., Langtry, R., and Völker, S., 2006. "Transition Modelling for General Purpose CFD Codes". *Flow, Turbulence and Combustion,* **77**(1), pp. 277–303.

[18] Maman, N., and Farhat, C., 1995. "Matching fluid and structure meshes for aeroelastic computations: A parallel approach". *Computers and Structures,* **54**(4), pp. 779–785.

[19] Farhat, C., Lesoinne, M., and Le Tallec, P., 1998. "Load and motion transfer algorithms for fluid/structure interaction problems with non-matching discrete interfaces: Momentum and energy conservation, optimal discretization and application to aeroelasticity". *Computer Methods in Applied Mechanics and Engineering,* **157**(1-2), pp. 95–114.

[20] Tezduyar, T., Sathe, S., Keedy, R., and Stein, K., 2006. "Space–time finite element techniques for computation of fluid–structure interactions". *Computer Methods in Applied Mechanics and Engineering,* **195**(17-18), pp. 2002–2027.